

Article

Five-Step Phase-Shift-Based Multiwavelength Averaging for Extrinsic Fabry–Perot Interferometric Sensors

Zheng Liu ^{1,2,†} , Qiong Yao ^{1,†}, Ji Xia ¹ , Gang Liu ^{1,2}, Shuidong Xiong ¹ and Qingkai Hou ^{1,*}

¹ College of Meteorology and Oceanography, National University of Defense Technology, Changsha 410073, China; liuzheng_01@nudt.edu.cn (Z.L.); yqnudt@nudt.edu.cn (Q.Y.); xiaji_2022@nudt.edu.cn (J.X.); lg_816@nudt.edu.cn (G.L.); xiong_shuidong@nudt.edu.cn (S.X.)

² College of Advanced Interdisciplinary Studies, National University of Defense Technology, Changsha 410073, China

* Correspondence: houkai7@nudt.edu.cn

† These authors contributed equally to this work.

Abstract: In order to address issues such as low demodulation accuracy, large demodulation errors, small dynamic range, and complex algorithms for the extrinsic Fabry–Perot interferometric (EFPI) sensor, a five-step phase-shift algorithm based on a multiwavelength (MW)-averaging method is proposed to improve demodulation speed, noise stability, dynamic range, and noise suppression. The proposed demodulation method utilizes white-light interferometry (WLI) technology to acquire the reflection spectra and extract the five-step phase-shift signals at N_s consecutive operating points. The demodulation results of N_s sets of five-step phase-shift signals are averaged to obtain the average demodulated phase and cavity length variation. Theoretical analysis demonstrates the significant effects of the MW demodulation method on demodulation parameter errors and noise suppression. Particularly, when the demodulation parameter $\theta = \pi/2$ rad, the method exhibits excellent stability against demodulation parameter error-induced instability. Moreover, it greatly improves noise suppression and reduces noise fluctuations. Numerical simulations are conducted to validate the performance of the proposed demodulation method. Compared with the traditional single-wavelength (SW) five-step phase-shifting demodulation method, the MW demodulation method exhibits stronger noise- and harmonic-suppression capabilities as the number of averaging wavelengths N_s increases. The harmonic distortion of the MW demodulation method with $N_s = 128$ is 20 dB lower than that of the SW demodulation method, and the noise is 15 dB lower. Furthermore, the proposed method effectively suppresses the influence of demodulation parameter errors on signal demodulation. This proposed demodulation method has the potential for fast real-time dynamic demodulation. It has great significance and application in the field of weak signal detection in fiber-optic sensors with interferometer structures and has enormous advantages in noise-suppression in complex environments.

Keywords: extrinsic Fabry–Perot interferometer (EFPI); five-step phase-shift algorithm demodulation; multiwavelength averaging; noise characteristic; numerical simulation



Citation: Liu, Z.; Yao, Q.; Xia, J.; Liu, G.; Xiong, S.; Hou, Q. Five-Step Phase-Shift-Based Multiwavelength Averaging for Extrinsic Fabry–Perot Interferometric Sensors. *Photonics* **2023**, *10*, 1076. <https://doi.org/10.3390/photonics10101076>

Received: 25 August 2023

Revised: 13 September 2023

Accepted: 18 September 2023

Published: 25 September 2023



Copyright: © 2023 by the authors. Licensee MDPI, Basel, Switzerland. This article is an open access article distributed under the terms and conditions of the Creative Commons Attribution (CC BY) license (<https://creativecommons.org/licenses/by/4.0/>).

1. Introduction

The fiber-optic extrinsic Fabry–Perot interferometric (EFPI) sensor [1,2] has become a research hotspot in the field of optical fiber sensing in recent years. When external parameters such as refractive index [3], temperature [4], or strain [5] change the length of the cavity or the reflectivity of the end face, the response of the resonant cavity changes. By measuring the spectrum, the corresponding physical quantities can be sensed. Since the introduction of the membrane-type EFPI [6] in the 1970s, various structures based on microelectromechanical systems (MEMS) [7–9] lithography and solution-etching methods have been proposed, using a collimating capillary structure [10]. Moreover, with the recent research on photonic crystal fibers [7,11], the structure of the resonant cavity has become more flexible and the

performance has become even more excellent. The significant advantage of EFPI is that the resonant cavity volume is extremely small [12], and it has a high sensitivity [13]. It can be made into a probe-type sensor for point-to-point measurements [14], realizing sensing of various parameters such as temperature [4], pressure [15], vibration [16], strain [17], chemical substances [18], and magnetic fields [19]. It has been successfully applied in large-scale building monitoring [20] and medical biology [21], as well as in industrial fields involving high temperatures [22], high pressure [23], and corrosion resistance [24].

The signal demodulation technology of fiber-optic sensors is a crucial component of a fiber-optic sensor system, and the performance of the demodulation system directly impacts the precision and speed of the demodulation of the whole sensor system. The demodulation of fiber EFPI sensor signals requires the analysis and processing of fiber interference spectra, necessitating the design of complex demodulation methods. These methods need to take into account the characteristics of fiber sensors and environmental noise, making the design and implementation of demodulation schemes intricate. Furthermore, high accuracy and demodulation stability are essential, demanding that the demodulation scheme should accurately extract the target information from the sensor signals while exhibiting strong suppression-capabilities against environmental noise and harmonic distortion. According to different demodulation concepts, the demodulation methods for EFPI sensors can be categorized into three types: intensity demodulation, wavelength demodulation, and phase demodulation. The underlying principle behind intensity demodulation is that, as the cavity length shifts as a result of measured external physical factors, the interference intensity of the EFPI sensor varies. The speed and simplicity of the demodulation process are the advantages of intensity demodulation, but its precision and dynamic range are constrained by the stability of the light-source. Typical intensity demodulation schemes include the working point-control method [25], dual-wavelength method [26], dual-cavity method [27,28], and so on. The dual-cavity approach was initially presented by Kent A. Murphy, and the dynamic strain is demodulated by two interference signals with a suitable phase orthogonal design [27]. To demodulate the fiber-optic EFPI sensors, a modified dual-cavity DC compensation approach is provided, which eliminates the need for matching between the cavities' difference and the light's wavelength [28]. Wavelength demodulation is acquired from wavelength information in the reflection spectrum, and the wavelength change is used to calculate the cavity length-change of the EFPI sensor. The major approaches are cavity length demodulation [29,30] and spectral peak tracking [31–33]. Some EFPI sensor spectra under a defined strain are analyzed so as to train a neural network, and the trained network is utilized to demodulate sensor strain [29]. The benefits of wavelength demodulation include its simple method and straightforward concept. However, it requires a large amount of spectral data if it is to be calculated, which is incompatible with high-frequency dynamic signal measurement. The key to phase demodulation is analyzing the phase-change of the EFPI sensor. It has a wide dynamic range, good demodulation accuracy, and high sensitivity, and it can demodulate dynamic signals well. For example, the phase-generated carrier (PGC) demodulation technique [16,34,35] comprises both internal and external modulation. The internal modulation technique modifies the phase of the light-source directly, and the light-source can be modulated at high frequency. The external modulation technique adds PZT to the sensing system, which has a relatively simple structure and minimal device needs, but it increases the system volume and weakens the system's anti-interference capacity. The phase-shift demodulation approach eliminates the impact of the DC component and fringe contrast in the interference signal; as a result, it is straightforward, robust, and extensively used. To reduce the impact of DC components, the three-wavelength phase-shift demodulation technique [36] employs the phase connection between the three interference signals, and the phase compensation algorithm generates two orthogonal signals to demodulate the tested signals being evaluated. Liu proposed a quasi-continuous quadrature frequency modulation, which utilizes a five-step phase-shift demodulation method and programmable frequency modulation to generate a continuous orthogonal phase-shift signal, successfully demodulating a 100 kHz ultrasound signal [37].

In the five-step phase-shifting algorithm based on the multiwavelength (MW) averaging method, the interference spectrum of EFPI sensors is obtained by white-light interference that is sampled at equal wavelength intervals. The spectral data is first processed by removing the spectrum envelope and elliptical fitting. When the reflection spectrum has N wavelengths, N_s ($0 < N_s \leq N - 4M$) groups of five-step phase-shift interference signals can be obtained. The phase connection between each group of five-step phase-shift interference signals is used to yield two orthogonal signals, and the changes in the beginning phase are derived using an arctangent algorithm. According to the relationship between phase and cavity length, averaging N_s groups of phase-changes can be utilized to determine the dynamic cavity length change of the EFPI sensor. Compared with the traditional five-step phase-shifted demodulation at a single wavelength (SW), here the five-step phase-shifted demodulation with MW demodulation can not only achieve fast dynamic demodulation over a wide dynamic range but can also effectively reduce noise and improve noise stability, as well as reducing the distortion influence of demodulated parameter errors on the demodulated signal.

2. Principle

Figure 1a illustrates the five-step phase-shift demodulation system with the MW demodulation method. Amplified spontaneous emission (ASE) acts as the light-source in this system. The signals emitted by ASE are directed through an isolator and circulator, and then pass through the EFPI sensor. The sensor reflects the signals, which again travel through the circulator before being received by the photodetector (PD). Finally, the signal is demodulated in real-time by a personal computer (PC).

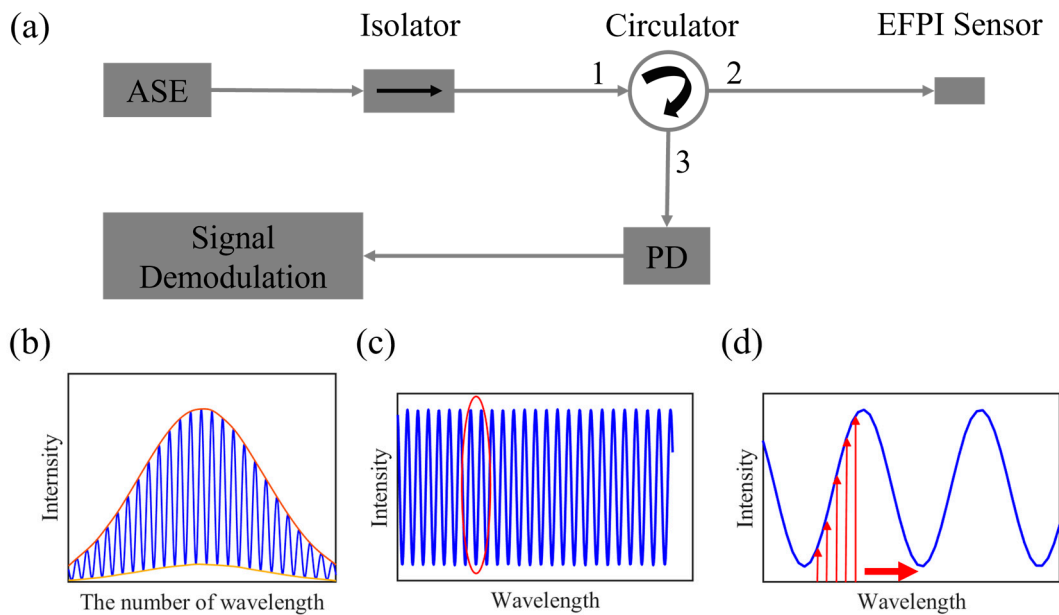


Figure 1. The working principle of the five-step phase-shift demodulation with MW averaging. (a) Schematic diagram of the five-step phase-shift demodulation with MW averaging. (b) Raw spectrum. The orange line and the yellow line represent the upper and lower envelopes of the spectrum, respectively. (c) Eliminate spectral envelope. (d) Zoom-in view of the eliminate spectral envelope in red circle. The upward arrow represents the extracted the five-step phase-shift signals. The rightward arrow indicates the direction for extracting the next set of five-step phase-shift signals.

The reflectivity of the two reflective surfaces of the EFPI sensor is minimal, so the interference of the sensor can be approximated to the dual-beam interference. Via sampling at equal intervals of the wavelength, with a wavelength interval $\Delta\lambda$, and a sampling length

N , the collected interference spectrum of the EFPI sensor is depicted in Figure 1b. The intensity of this spectrum can be expressed as follows

$$I = A + B \cos\left(\frac{4\pi L}{\lambda}\right), \tag{1}$$

where A is the direct current (DC) of the interference signal, B is the alternating current (AC) of the interference signal, and L is the cavity length.

The spectrum is modified by the minimax method, and Figure 1c shows the correcting reflection spectrum $I' = \cos(4\pi L/\lambda)$. The intensity of λ_{k-2M} , λ_{k-M} , λ_k , λ_{k+M} , and λ_{k+2M} as a group of five-step phase-shift signals is extracted from I' ($k = 2M + 1, 2M + 2, \dots, N - 2M - 1$). M is the wavelength interval ($0 < M \leq N/5$), and λ_k is the working point of the five-step phase-shift method. The five-step phase-shift signals could be written as

$$\begin{cases} I'_{k1} = \cos(\varphi_k - 2\theta_k) \\ I'_{k2} = \cos(\varphi_k - \theta_k) \\ I'_{k3} = \cos(\varphi_k) \\ I'_{k4} = \cos(\varphi_k + \theta_k) \\ I'_{k5} = \cos(\varphi_k + 2\theta_k) \end{cases}, \tag{2}$$

where $\varphi_k = 4\pi L/\lambda_k$, $\theta_k = -4\pi L \cdot M\Delta\lambda/\lambda_k^2$. Ns groups of five-step phase-shift signals can be extracted from I' with N wavelengths ($0 < Ns \leq N - 4M$), as shown in Figure 1d.

To generate two orthogonal signals, the phase connection between each group of five-step phase-shift interference signals is utilized. The arctangent algorithm is used to obtain the demodulation phase, expressed as

$$\varphi_k = \arctan\left(\frac{SR_k}{CR_k}\right), \tag{3}$$

where $SR_k = (I'_{k2} \vee I'_{k4})/2\sin\theta_k$ and $CR_k = (2I'_{k3} - I'_{k1} - I'_{k5})/4\sin^2\theta_k$. The demodulated parameter θ_k is obtained through ellipse fitting of correcting reflection spectrum I' . Moreover, $\varphi_k = 4\pi L/\lambda_k$ is used to determine the change in cavity length at λ_k , which can be described as

$$dL_k = \frac{d\varphi_k \lambda_k}{4\pi}, \tag{4}$$

The dynamic cavity length variation can be obtained by averaging the demodulation results at MW demodulation, and it can be rewritten as

$$dL = \overline{dL_k}, \tag{5}$$

In the measurements, the result of SW demodulation indicates cosine variation with different working point positions. MW demodulation averages the results of multiple working points, avoiding the impact of the working point shift on the demodulation results.

3. Demodulated Phase Error Analysis

The light signal is emitted from the ASE through an optical circuit, then reflected by EFPI sensors, and collected using PD and A/D conversion. In addition to the external target-sensing information, the demodulated signal also contains noise that is induced by both the fluctuation of the light-source (multiplicative noise) and the back-end signal processing circuit (additive noise). Light intensity fluctuation can also cause an error in the demodulated parameter θ , which is defined as the difference between the actual demodulated parameter and its true value, denoted as $\Delta\theta$. By examining Equation (3), it becomes apparent that any error $\Delta\theta$ in the demodulated parameter θ will cause a disruption in the demodulation phase φ_k , leading to a distortion in the ultimate outcome. Furthermore,

both Equations (4) and (5) demonstrate that the final demodulation phase is dependent on the intensity and demodulated parameter θ . Consequently, the impact of the following three parameters (namely demodulated parameter error, multiplicative noise, and additive noise) on the demodulation phase are analyzed.

3.1. Demodulated Parameter Error

According to Equation (3), the demodulated parameter θ determines the accuracy of the demodulated phase. When the demodulated parameter θ includes an error $\Delta\theta$, the phase error of SW demodulation is solved from Equation (3)

$$\delta\varphi = \frac{1}{2} \sin 2\varphi \left(-\frac{\Delta\theta^2}{2} + \frac{\Delta\theta}{\tan \theta} \right), \tag{6}$$

An average effect is produced after MW demodulation, which suppresses the demodulation phase error. The phase error of MW demodulation is written as

$$\overline{\Delta\varphi} = \frac{1}{2} \frac{\sum_k^{N-4M} \sin 2\varphi_k}{N-4M} \left(-\frac{\Delta\theta^2}{2} + \frac{\Delta\theta}{\tan \theta} \right), \tag{7}$$

As indicated in Equation (7), the demodulated parameter θ and the demodulated parameter error $\Delta\theta$ do not change after MW averaging, in comparison to SW demodulation. However, the demodulated phase φ yields an average value. The three factors, including the demodulated parameter θ , the demodulated parameter error $\Delta\theta$, and the demodulated phase φ , together determine the demodulated phase error $\delta\varphi$. To demonstrate the effect of these three factors on the demodulation phase, a numerical simulation is conducted utilizing Equations (6) and (7), and the results are presented in Figure 2.

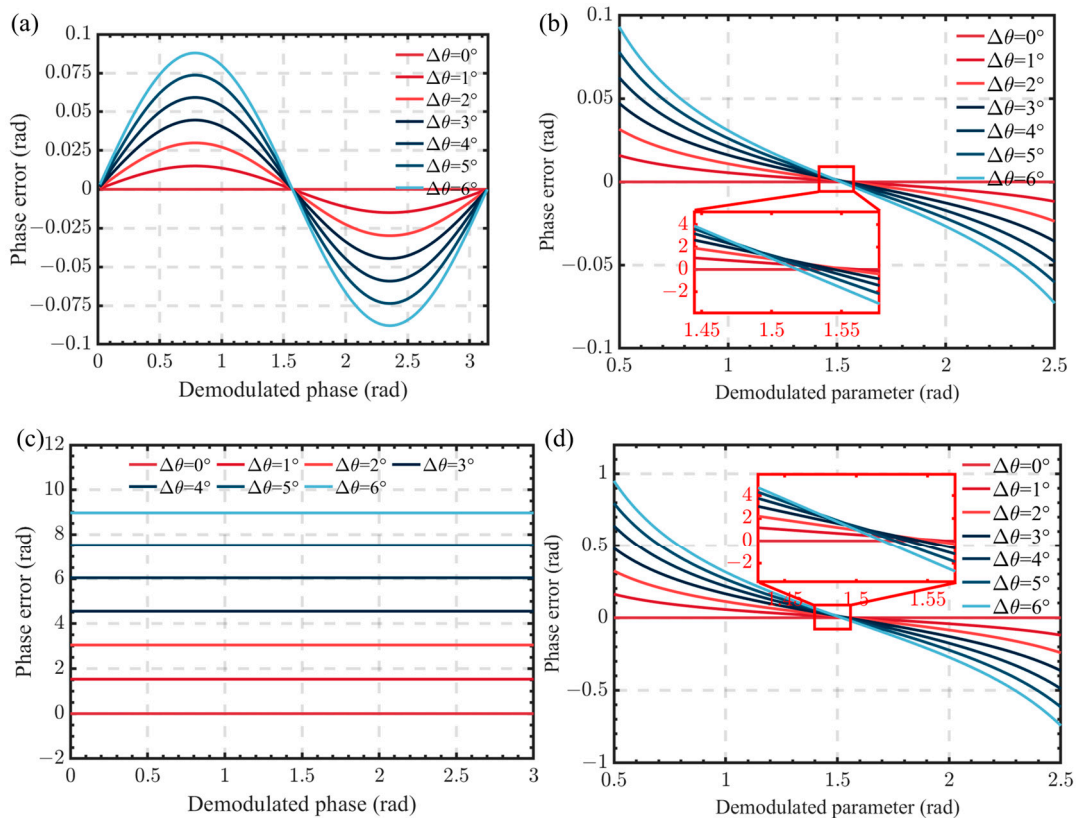


Figure 2. Simulation result for demodulated parameter error with demodulated phase φ , demodulated parameter θ , and demodulated parameter error $\Delta\theta$. (a,b) SW demodulation. (c,d) MW demodulation.

Comparing Figure 2a,c reveals that the demodulated phase error $\delta\varphi$ of the SW demodulation method is sinusoidal with a period of π rad as the demodulated phase φ changes. On the other hand, the demodulated phase error remains constant with the change of demodulated phase φ after the MW demodulation method. In both SW and MW demodulation methods, the phase error steadily increases as the demodulated parameter error $\Delta\theta$ increases. Comparing Figure 2b,d shows that the demodulated phase error $\delta\varphi$ of both SW and MW demodulation methods tends to decrease initially and then increase with the increase of demodulated parameter θ . However, the MW demodulation method is more effective in reducing the demodulated phase error caused by the demodulated parameter error $\Delta\theta$, which is 19 orders of magnitude lower than that of the SW demodulation method. Therefore, setting an optimized wavelength interval M , and configuring the demodulated parameter θ as $\pi/2$ rad, is an effective approach to reducing the phase error caused by the demodulated parameter error $\Delta\theta$.

3.2. Multiplicative Noise

Multiplicative noise is typically attributed to fluctuations in the light-source, and it coexists with the signal in a multiplied form. In order to simplify the analysis, this paper adopts an approach that assumes uncorrelated multiplicative noise.

Without considering the demodulated parameter error, and assuming the uncorrelated multiplicative noise coefficient is n_{k-i} ($i = 1\sim 5$), Equation (2) can be written as

$$I'_{ki} = I_{ki} + \delta I_{ki}, \tag{8}$$

where $I_{ki} = A_k + B_k \cos(\varphi_k \pm m\theta_k)$, $\delta I_{ki} = n_{k-i} I_{ki}$, $m = 0, 1, 2$.

Assuming that the DC and AC of the interference signal are $A_k = A$ and $B_k = B$, the phase error of SW demodulation can be derived from Equation (3) as

$$\delta\varphi \approx \cos\varphi \frac{n_{k-2}I_2 - n_{k-4}I_4}{2B \sin\theta} - \sin\varphi \frac{2n_{k-3}I_3 - n_{k-1}I_1 - n_{k-5}I_5}{4B \sin^2\theta}, \tag{9}$$

Calculating the noise-power spectrum and assuming that the uncorrelated multiplicative noise-power coefficient is $S_\omega(n_{k-i}) = S_\omega(n_k)$ ($i = 1\sim 5$), then Equation (9) can be written as

$$S_\omega(\delta\varphi) = S_\omega(n_k) \left[\cos^2\varphi \frac{I_2^2 + I_4^2}{4B^2 \sin^2\theta} + \sin^2\varphi \frac{4I_3^2 + I_1^2 + I_5^2}{16B^2 \sin^4\theta} \right], \tag{10}$$

The noise-power spectrum of MW demodulation is written as

$$\overline{S_\omega(\delta\varphi)} = \frac{1}{N - 4M} S_\omega(n_k) \left[\sum_k^{N-4M} \cos^2\varphi \frac{I_2^2 + I_4^2}{4B^2 \sin^2\theta} + \sum_k^{N-4M} \sin^2\varphi \frac{4I_3^2 + I_1^2 + I_5^2}{16B^2 \sin^4\theta} \right], \tag{11}$$

As depicted in Equations (10) and (11), the noise-power spectrum resulting from uncorrelated multiplicative noise is influenced by the DC and AC components of the interference signal, the demodulated phase φ , and the demodulated parameter θ . For the sake of simplicity in analysis, assume that $A = 0$, $B = 1$, and $S_\omega(n_k) = 0.2$. The numerical simulation results are presented in Figure 3.

Figure 3 reveals that, as the demodulated parameter θ approaches $\pi/2$ rad, the fluctuations in the noise-power spectrum caused by the demodulated phase changes gradually diminish for both SW demodulation and MW demodulation methods. In comparison with the SW demodulation method, the noise-power spectrum of uncorrelated multiplicative noise experiences a reduction of approximately 45 dB.

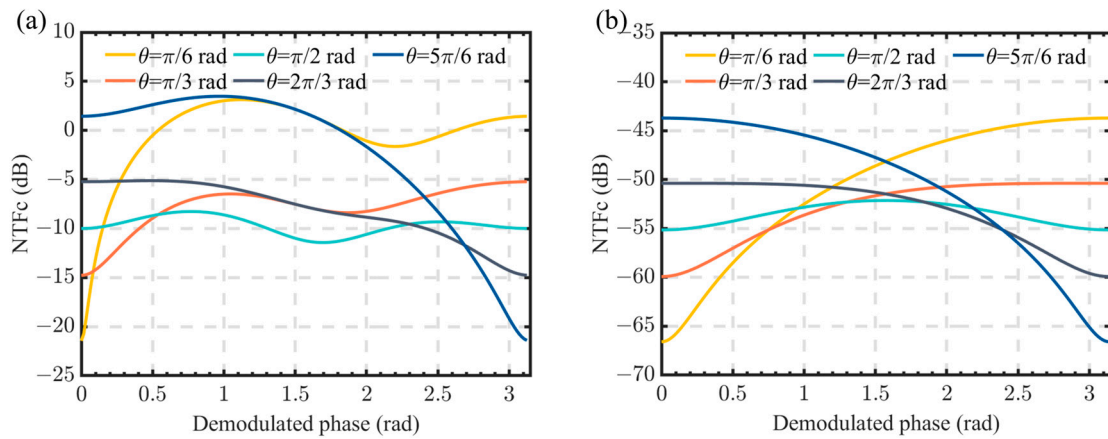


Figure 3. Simulation result for the noise-power spectrum caused by uncorrelated multiplicative noise with demodulated phase φ , demodulated parameter θ . (a) SW demodulation. (b) MW demodulation.

3.3. Additive Noise

Additive noise encompasses various types such as thermal noise and shot noise. It is characterized by its additive relationship with the signal, persisting irrespective of the presence of the signal. In order to streamline the analysis, the theoretical analysis of additive noise-suppression in this article primarily focuses on the impact of circuit noise within uncorrelated additive noise on the amplitude of light intensity.

Without considering the demodulated parameter error, and assuming the uncorrelated multiplicative noise coefficient is n_{k-i} ($i = 1\sim 5$), Equation (2) can be written as

$$I'_{ki} = I_{ki} + n_{d-i}, \tag{12}$$

where $I_{ki} = A_k + B_k \cos(\varphi_k \pm m\theta_k)$, $m = 0, 1, 2$.

Assuming that the DC and AC of the interference signal are $A_k = A$ and $B_k = B$, the demodulated phase error $\delta\varphi$ of SW demodulation is obtained by Equation (3)

$$\delta\varphi \approx \frac{\cos \varphi}{2B \sin \theta} (n_{d-2} - n_{d-4}) - \frac{\sin \varphi}{4B \sin^2 \theta} (2n_{d-3} - n_{d-1} - n_{d-5}), \tag{13}$$

Calculating the noise-power spectrum and assuming that the uncorrelated additive noise-power coefficient is $S_\omega(n_{d-i}) = S_\omega(n_d)$ ($i = 1\sim 5$), Equation (13) can be written as

$$S_\omega(\delta\varphi) = \frac{1}{B^2} S_\omega(n_d) \left(\frac{\cos^2 \varphi}{2 \sin^2 \theta} + \frac{3 \sin^2 \varphi}{8 \sin^4 \theta} \right), \tag{14}$$

The noise-power spectrum of MW demodulation is written as

$$\overline{S_\omega(\delta\varphi)} = \frac{1}{B^2} S_\omega(n_d) \frac{1}{N-4} \left(\frac{\sum_k^{N-4M} \cos^2 \varphi_k}{2 \sin^2 \theta} + \frac{3 \sum_k^{N-4M} \sin^2 \varphi_k}{8 \sin^4 \theta} \right), \tag{15}$$

As shown in Equations (14) and (15), the noise-power spectrum caused by uncorrelated additive noise is related to the effects of AC, the demodulated phase φ , and the demodulated parameter θ . To simplify the analysis, assume that $B = 1$ and $S_\omega(n_d) = 0.2$. The numerical simulation is shown in Figures 4 and 5.

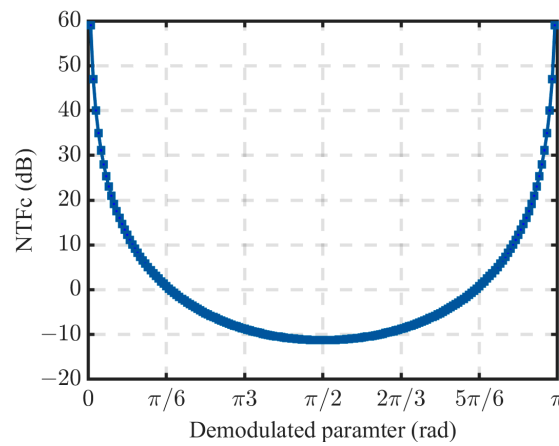


Figure 4. The noise-power spectrum changes with the demodulation parameter ($\varphi = \pi/2$ rad).

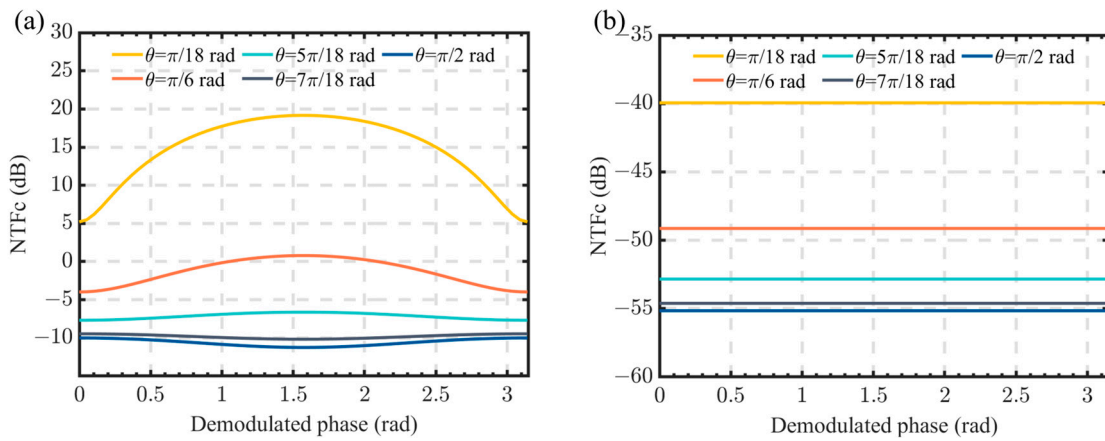


Figure 5. Simulation result for the noise-power spectrum caused by uncorrelated additive noise with demodulated phase φ , demodulated parameter θ . (a) SW demodulation. (b) MW demodulation.

Figure 4 illustrates that the noise-power spectrum of uncorrelated additive noise reaches its lowest point at the demodulated parameter $\theta = \pi/2$ rad, and increases as θ deviates from $\pi/2$ rad. Similarly, Figure 5 demonstrates that the noise-power spectrum of uncorrelated noise gradually decreases as θ equals or approaches $\pi/2$ rad. When comparing Figure 5a with Figure 5b, it is observed that the noise level of MW demodulation decreases by approximately 40 dB and remains unaffected by changes in the demodulated phase φ . MW demodulation proves to be effective in mitigating the impact of uncorrelated additive noise on signal demodulation.

4. Simulation

Without doubt, both dynamic range and noise characteristics are crucial factors in evaluating a demodulation method. It is important to focus on the harmonic-suppression capability of MW demodulation during signal demodulation within the dynamic range. Additionally, the noise spectrum level and noise stability under different parameter conditions such as the number of averaging wavelength N_s , the demodulated parameter θ , and the signal-to-noise ratio (SNR) should be considered. As depicted in Equation (3), it is evident that the demodulated parameter θ significantly impacts the accuracy of the demodulation method. The capability of the proposed demodulation method to suppress the impact caused by the demodulated parameter error $\Delta\theta$ should also serve as a criterion for assessing demodulation performance. Efficient elimination of the demodulated parameter error $\Delta\theta$ leads to more precise demodulation results. To investigate the effect of the demodulated phase error $\delta\varphi$ induced by the above parameters, numerical simulations are

conducted to analyze the influence of the dynamic range, demodulated parameter θ , and noise characteristics on the proposed interrogation method.

4.1. Dynamic Range

According to Equation (3), the dynamic range of the proposed method is determined by the arctangent algorithm. The dynamic range ΔL_{\max} can be expressed as

$$\begin{cases} \varphi_{\max} = \frac{f_p}{2f_s} \\ \varphi = \frac{4\pi\Delta L}{\lambda} \end{cases} \Rightarrow \Delta L_{\max} = \frac{f_p}{2f_s} \cdot \frac{\lambda}{4\pi}, \quad (16)$$

where φ_{\max} is the maximum signal phase that the demodulation method can resolve efficiently, the corresponding maximum demodulated cavity length variation is ΔL_{\max} , the system sampling frequency is f_p , and the signal frequency is f_s . It can be seen in Equation (16), that the dynamic range of the demodulation method is proportional to $1/2 f_s$, and the numerical simulation of Equation (16) is calculated as shown in Figure 6.

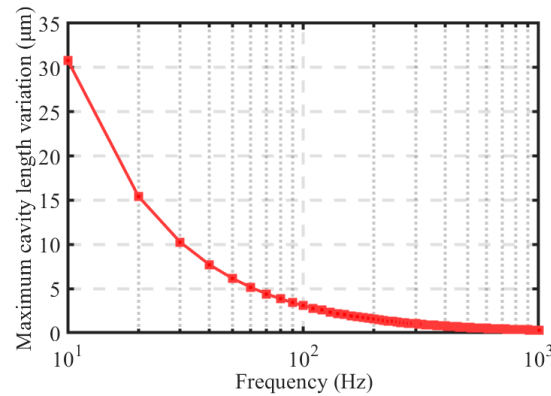


Figure 6. Simulated result for dynamic range of the demodulation method.

Figure 6 demonstrates that the maximum cavity length variation ΔL_{\max} decreases as the signal frequency increases, assuming constant sampling and incident light wavelength. When the cavity length changes beyond the dynamic range, it can result in distortion or even failure of signal demodulation. Hence, it is crucial to analyze the demodulation method’s dynamic range for practical measurements and applications. Distortion of the resolved signal is not solely caused by the dynamic range but can also be induced by harmonic signals stemming from the nonlinearity of the sensing system. The influence of harmonic signals on the fundamental signal is a customized way of assessing the demodulation method’s quality. The total harmonic distortion (THD) is defined as the ratio of the sum of all harmonic signals to the fundamental signal.

Numerical simulations of THD in five-step phase-shift demodulation with SW demodulation and MW demodulation methods are presented in Figure 7. For the purpose of comparing the results, the number of averaging wavelengths in MW demodulation is simplified as 16, 32, 64, and 128 wavelengths. Considering the current measurement conditions to avoid the influence of the 50 Hz power signal, the simulation parameters are set as a sampling frequency 5 kHz, signal frequency 63 Hz to be measured, as well as an $M = 1$ wavelength interval. In addition, the wavelength range of the light-source is set to 1506–1592 nm, the sampling length is set to $N = 512$, and the signal-to-noise ratio is 80 dB. To avoid the distortion caused by signal demodulation beyond the dynamic range, simulation should be conducted within the dynamic range. According to Equation (16), the maximum phase amplitude that can be achieved in the proposed demodulation method is $\varphi_{\max} = 39.7$ rad; the changes in THD with the phase-amplitude of the signal are shown in Figure 7.

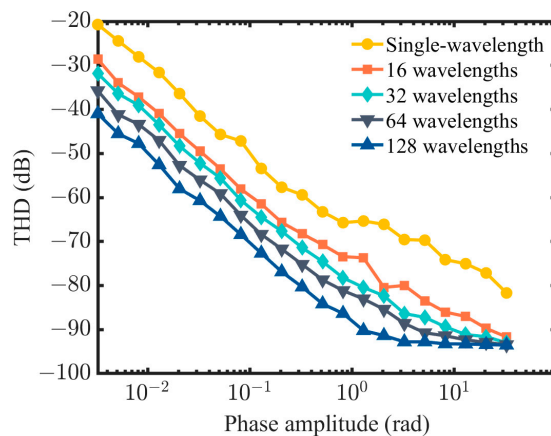


Figure 7. The changes in THD with phase-amplitude of the signal.

As shown in Figure 7, it is apparent that the THD of both the SW demodulation method and MW demodulation method gradually decreases with the increase of signal phase-amplitude. When the signal phase-amplitude is close to the maximum phase-amplitude, the THD of MW demodulation gradually approaches the noise spectrum level, and the THD of different MW demodulations gradually approaches the noise spectrum level. Compared to SW demodulation, the THD of MW demodulation is much lower. For example, the THD of 128 wavelengths demodulation is 20 dB lower than that of SW demodulation. As shown in Figures 2, 3 and 5, it can be seen that the results of the SW demodulation method under different working points are averaged by the MW demodulation method, avoiding the impact of the working point fluctuations and effectively reducing noise levels. With the increase of averaging wavelength number, the average processing of the MW demodulation method plays a significant role in contributing to the gradually decreased THD. Furthermore, the proposed demodulation method shows the advantages of signal demodulation in complex environments, such as its ability to efficiently suppress harmonics and the detection of weak signals.

4.2. Demodulated Parameter Error

The demodulated parameter θ in the proposed method is calculated by ellipse fitting, and its theoretical value can be expressed as $\theta = -4\pi L \cdot M \Delta\lambda / \lambda^2$. When the demodulated parameter θ has an error $\Delta\theta$, it will affect the accuracy of the demodulated phase φ and could lead to distortion of the signal. Let us analyze the impact of the demodulated parameter error $\Delta\theta$ on signal demodulation distortion, as well as the impact of the different demodulated parameter θ on harmonic suppression. The simulation parameters are chosen as: demodulated parameter error $\Delta\theta = 0^\circ, 1^\circ, 2^\circ, 3^\circ, 4^\circ, 5^\circ$, and 6° , $\Delta L = 100$ nm, the number of averaging wavelengths is 64, wavelength interval $M = 1, 3, 5, 7$ and 9 (corresponding theoretical demodulated parameter $\theta = 0.3151, 0.9451, 1.5750, 2.2043$ and 2.8329 rad). The numerical simulation is resolved as shown in Figure 8.

Figure 8 demonstrates how the MW demodulation method can effectively mitigate the distortion caused by the demodulated parameter error $\Delta\theta$ compared to the SW demodulation method. Compared with the SW demodulation method, the THD of the MW demodulation method is lower by 20~30 dB in similar conditions. The THD has a relationship with wavelength interval M that THD can reach a minimum when $M = 5$ ($\theta = 1.5750$ rad). Therefore, as the demodulated parameter θ is close to $\pi/2$ rad, the harmonic distortion is substantially decreased and suppressed. As the demodulated parameter error $\Delta\theta$ increases, the THD of SW demodulation and MW demodulation methods gradually increases. However, the THD does not change with the demodulated parameter error $\Delta\theta$ when $M = 5$. It is consistent with the theoretical result in Figure 2, where the phase error is 0 at $\theta = \pi/2$ rad and it is independent of the amplitude of the demodulated parameter error. Except for the curve with a wavelength interval of $M = 5$, the results of other curves in Figure 8 differ

from their expected trends when $\Delta\theta = 0^\circ$. This is because when $\Delta\theta \neq 0^\circ$, the proposed demodulation method is mainly affected by the demodulated parameter error. When $\Delta\theta = 0^\circ$, the impact of other parameters such as the number of averaging wavelengths and the wavelength interval M on the demodulation results becomes apparent.

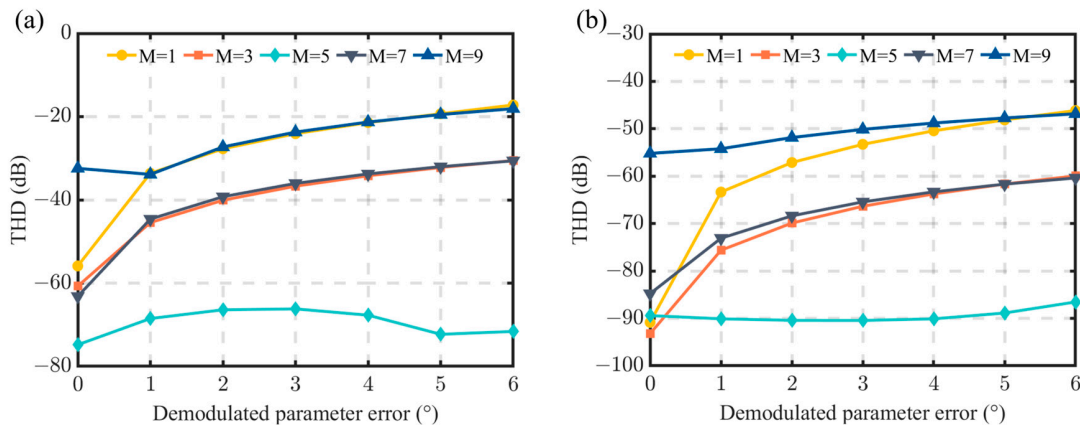


Figure 8. The influence of demodulated parameter error $\Delta\theta$ and demodulated parameter θ in distortion of signal demodulation. (a) SW demodulation. (b) MW demodulation.

4.3. Noise Characteristics

The analysis in this paper covers three main aspects regarding noise characteristics. Firstly, it examines the demodulation noise level at different SNRs. In particular, it investigates the challenges of accurately measuring weak signals for sensing purposes under low-SNR conditions. It is crucial to analyze these noise characteristics to offer practical guidance. Secondly, the relationship between the fluctuation of demodulation noise level in the SW demodulation method and the wavelength interval M is investigated. The selection of the working point and wavelength interval M substantially impacts the results obtained through the SW demodulation method. Lastly, the relationship between the demodulation noise level in the MW demodulation method and the number of averaged wavelengths, along with the wavelength interval M , is explored. Unlike the SW demodulation method, the MW demodulation method overcomes the influence of the working point on the demodulation results by implementing an averaging procedure. By conducting a comprehensive analysis of the noise characteristics in both SW and MW demodulation methods, it is possible to effectively suppress noise and harmonic distortion in practical applications. The MW demodulation method employs five-step phase-shift signals with multiple wavelengths. For instance, the case of 64-wavelengths demodulation includes 64 groups of five-step phase-shift signals. Figures 9 and 10 illustrate the results of different SW and MW demodulation methods, respectively.

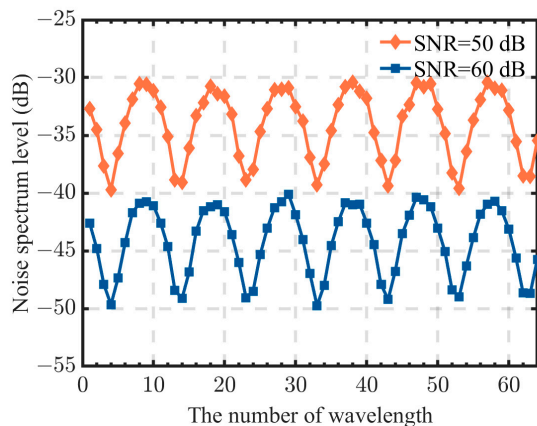


Figure 9. The noise spectrum level of SW demodulation with different working points and SNR.

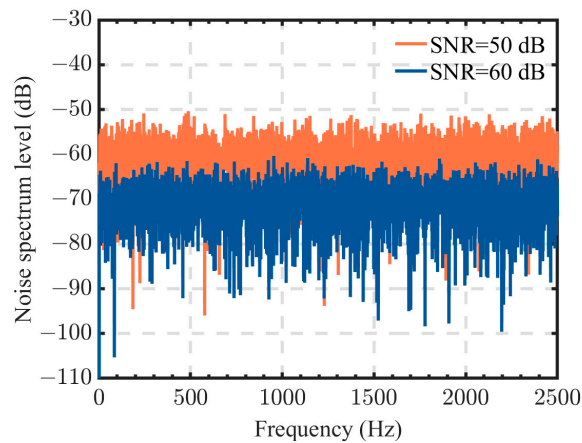


Figure 10. The noise spectrum level of MW demodulation with different SNR.

With the change in working point, the noise spectrum level of the SW demodulation method displays periodic fluctuation, as shown in Figure 9. In practical applications, determining the cavity length of the EFPI sensor is necessary to ensure that the working point operates at an optimal demodulation position. However, this can impede the fast demodulation of the sensing signal. Both Figures 9 and 10 demonstrate that the noise spectrum level of both SW and MW demodulation methods decreases to 10 dB when the SNR changes from 50 dB to 60 dB. Compared to the SW demodulation method, the MW demodulation method exhibits a noise spectrum level approximately 20 dB to 25 dB lower at the same SNR, making it more advantageous for detecting weak signals in complex environmental conditions.

According to the expression $\theta = -4\pi L \cdot M \Delta\lambda / \lambda^2$, the SW demodulation and MW demodulation are correlated with the wavelength interval M . The previous analysis has summarized the relationship between the noise spectral level of the method, the operating point and SNR, and has given the characteristics of the noise spectral level under different wavelength intervals. The relationship between the fluctuation of the SW demodulation noise spectrum and wavelength interval M is further analyzed. The simulation parameters are wavelength interval $M = 1, 3, 5, 7, \text{ and } 9$.

As shown in Figure 11, as the demodulated parameter θ approaches $\pi/2$ rad ($M = 5$), the noise spectrum level of SW demodulation is lower, and the stability of the noise level behaves much better. By contrast, when the demodulated parameter θ moves away from $\pi/2$ rad ($M < 5$ or $M > 5$), the periodic variation of SW noise fluctuation is much higher; with the change in wavelength number, there is remarkable periodic fluctuation.

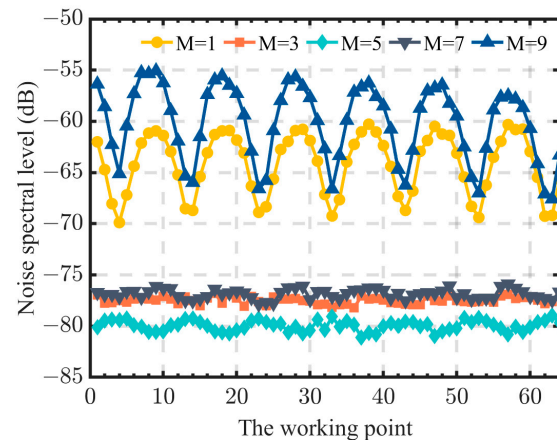


Figure 11. The noise spectrum level of SW demodulation with different working points and wavelength intervals M .

The MW demodulation greatly eliminates the impact of the working point on the demodulation results. The impact of wavelength interval M and the number of averaging wavelengths on MW demodulation still needs further analysis; the noise spectrum level of MW demodulation with different wavelength intervals M and different numbers of averaging wavelengths is shown in Figure 12. With the increase of averaging wavelengths number, the noise spectrum level gradually decreases. For example, when wavelength interval $M = 1$, as the number of averaged wavelengths increases from 1 to 128, the noise spectral level decreases by about 30 dB. With the demodulated parameter θ approaching $\pi/2$ rad ($M = 5$), the noise spectrum level of MW demodulation is lower. As shown in Figure 4, it can be seen that, as the demodulated parameter θ approaches $\pi/2$ rad, the corresponding noise-power spectrum decreases slowly. This is consistent with the conclusion in Figure 12 that the noise spectrum level in the cases of $M = 3$ and $M = 7$ is similar to the noise spectrum level of $M = 5$. This is consistent with the theoretical analysis results. In particular, when the averaging wavelength number is small, the difference in noise spectrum level between different wavelength intervals is more obvious.

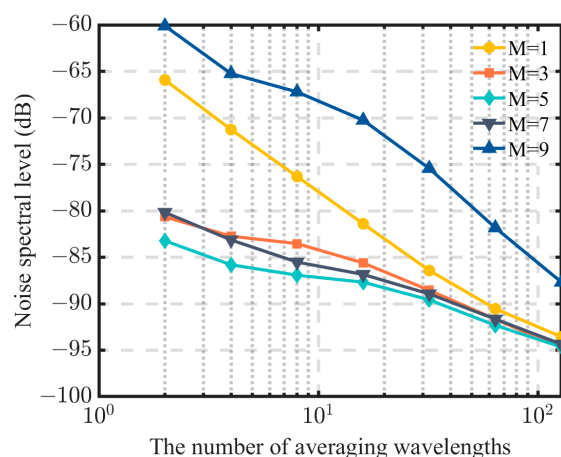


Figure 12. The noise spectrum level of MW demodulation with different numbers of averaging wavelengths and wavelength intervals M .

5. Conclusions

In summary, this manuscript presents a five-step phase-shift technique based on MW-averaging for fast real-time dynamic demodulation of the EFPI sensor. The principle of the five-step phase-shift technique based on MW-averaging is analyzed, and the impact of reducing the demodulated parameter error $\Delta\theta$ on signal-demodulation and noise-suppression is derived from three aspects, including the demodulated parameter error $\Delta\theta$, multiplicative noise, and additive noise. It is demonstrated that MW demodulation outperforms SW demodulation in reducing the impact of the demodulated parameter error $\Delta\theta$ on signal-demodulation and noise-suppression. The proposed demodulation method shows promise for fast real-time dynamic demodulation, making it suitable for various applications in the field of weak signal detection using fiber-optic sensors with interferometer structures. Additionally, the MW demodulation method exhibits stronger noise- and harmonic-suppression capabilities as the number of averaging wavelengths N_s increases. This suggests that the demodulation method can be further optimized and extended by exploring the use of more wavelengths for averaging, potentially enhancing its performance in noise reduction and signal stability. Overall, the proposed method offers improved demodulation speed, noise stability, dynamic range, and noise-suppression, making it a promising technique for various sensing applications. It has the potential to revolutionize the field of EFPI sensors and to contribute to advancements in weak signal-detection and noise-reduction in complex environments.

Author Contributions: Conceptualization, Z.L. and Q.Y.; methodology, Z.L., Q.Y., J.X. and Q.H.; software, Z.L., Q.Y. and G.L.; investigation, Z.L., G.L. and S.X.; resources, S.X. and Q.H.; writing—original draft preparation, Z.L., Q.Y., J.X. and Q.H.; writing—review and editing, S.X. and Q.H.; supervision, Q.H.; funding acquisition, S.X. All authors have read and agreed to the published version of the manuscript.

Funding: This research was funded by the National Defense Science and Technology Foundation Enhancement Program (173 Key Program), grant number 2019-JCJQ-ZD-026-00.

Institutional Review Board Statement: Not applicable.

Informed Consent Statement: Not applicable.

Data Availability Statement: The data that support the findings of this study are available from the corresponding author upon reasonable request.

Conflicts of Interest: The authors declare no conflict of interest.

References

1. Wang, S.; Zhang, J.; Xu, H.; Yao, Q.; Chen, Y.; Lu, P.; Liu, L.; Liao, H.; Sun, Y.; Ni, W.; et al. An Infrasound Sensor Based on Extrinsic Fiber-Optic Fabry–Perot Interferometer Structure. *IEEE Photonics Technol. Lett.* **2016**, *28*, 1264–1267. [[CrossRef](#)]
2. Liu, Y.; Jing, Z.; Li, R.; Zhang, Y.; Liu, Q.; Li, A.; Zhang, C.; Peng, W. Miniature fiber-optic tip pressure sensor assembled by hydroxide catalysis bonding technology. *Opt. Express* **2020**, *28*, 948–958. [[CrossRef](#)]
3. Yang, D.; Liu, Y.; Wang, Y.; Zhang, T.; Shao, M.; Yu, D.; Fu, H.; Jia, Z. Integrated optic-fiber sensor based on enclosed EFPI and structural phase-shift for discriminating measurement of temperature, pressure and RI. *Opt. Laser Technol.* **2020**, *126*, 106112. [[CrossRef](#)]
4. Liu, T.; Yin, J.; Jiang, J.; Liu, K.; Wang, S.; Zou, S. Differential-pressure-based fiber-optic temperature sensor using Fabry–Perot interferometry. *Opt. Lett.* **2015**, *40*, 1049–1052. [[CrossRef](#)] [[PubMed](#)]
5. Ramakrishnan, M.; Rajan, G.; Semenova, Y.; Farrell, G. Overview of Fiber Optic Sensor Technologies for Strain/Temperature Sensing Applications in Composite Materials. *Sensors* **2016**, *16*, 99. [[CrossRef](#)] [[PubMed](#)]
6. Zhao, M.; Jiang, K.; Bai, H.; Wang, H.; Wei, X. A MEMS based Fabry–Perot accelerometer with high resolution. *Microsyst. Technol.* **2020**, *26*, 1961–1969. [[CrossRef](#)]
7. Nie, Y.; Huang, K.; Yang, J.; Cao, L.; Cheng, L.; Wang, Q.; Tian, H.; Peihua, W.; Heng, L. A Proposal to Enhance High-Frequency Optical MEMS Accelerometer Sensitivity Based on a One-Dimensional Photonic Crystal Wavelength Modulation System. *IEEE Sens. J.* **2020**, *20*, 14639–14645. [[CrossRef](#)]
8. Shotorban, A.K.N.; Jafari, K.; Abedi, K. Optical MEMS accelerometer sensor relying on a micro-ring resonator and an elliptical disk. *IET Circuits Devices Syst.* **2019**, *13*, 1102–1106. [[CrossRef](#)]
9. Zandi, K.; Belanger, J.A.; Peter, Y.-A. Design and Demonstration of an In-Plane Silicon-on-Insulator Optical MEMS Fabry–Perot-Based Accelerometer Integrated with Channel Waveguides. *J. Microelectromech. Syst.* **2012**, *21*, 1464–1470. [[CrossRef](#)]
10. Corres, J.M.; Bravo, J.; Arregui, F.J.; Matias, I.R. Vibration monitoring in electrical engines using an in-line fiber etalon. *Sens. Actuators A Phys.* **2006**, *132*, 506–515. [[CrossRef](#)]
11. Sheikhalah, A.; Abedi, K.; Jafari, K. A Proposal for an Optical MEMS Accelerometer Relied on Wavelength Modulation With One Dimensional Photonic Crystal. *J. Light. Technol.* **2016**, *34*, 5244–5249. [[CrossRef](#)]
12. Liu, B.; Zhou, H.; Liu, L.; Wang, X.; Shan, M.; Jin, P.; Zhong, Z. An Optical Fiber Fabry–Perot Microphone Based on Corrugated Silver Diaphragm. *IEEE Trans. Instrum. Meas.* **2018**, *67*, 1994–2000. [[CrossRef](#)]
13. Gong, Z.; Chen, K.; Zhou, X.; Yang, Y.; Zhao, Z.; Zou, H.; Yu, Q. High-Sensitivity Fabry–Perot Interferometric Acoustic Sensor for Low-Frequency Acoustic Pressure Detections. *J. Light. Technol.* **2017**, *35*, 5276–5279. [[CrossRef](#)]
14. Liu, Q.; Li, A.; Liu, Y.; Jing, Z.; Peng, W. TWDM-Assisted Active Quadrature Demodulation of Fiber-Optic Fabry–Perot Acoustic Sensor Network. *J. Light. Technol.* **2021**, *39*, 3991–3997. [[CrossRef](#)]
15. Tian, B.; Zhan, F.; Han, F.; Li, K.; Zhao, N.; Yang, N.; Jiang, Z. An optical fiber Fabry–Perot micro-pressure sensor based on beam-membrane structure. *Meas. Sci. Technol.* **2018**, *29*, 125104. [[CrossRef](#)]
16. Jia, P.G.; Wang, D.H. Self-calibrated non-contact fiber-optic Fabry–Perot interferometric vibration displacement sensor system using laser emission frequency modulated phase generated carrier demodulation scheme. *Meas. Sci. Technol.* **2012**, *23*, 115201. [[CrossRef](#)]
17. Claus, R.O.; Tuck, C.J.; Fernando, G.F.; Spillman, J.W.B. Multiplexed optical fiber Fabry–Perot sensors for strain metrology. In Proceedings of the Smart Structures and Materials 1999: Sensory Phenomena and Measurement Instrumentation for Smart Structures and Materials, Newport Beach, CA, USA, 31 May 1999; pp. 322–329.
18. Hungund, A.P.; Zhang, B.; Nambisan, A.; Naku, W.; Il, R.E.G.; Huang, J. Chemical Classification by Monitoring Liquid Evaporation Using Extrinsic Fabry–Perot Interferometer with Microwave Photonics. *J. Light. Technol.* **2023**, 1–14. [[CrossRef](#)]
19. Feng, X.; Jiang, Y.; Zhang, H. A mechanical amplifier based high-finesse fiber-optic Fabry–Perot interferometric sensor for the measurement of static magnetic field. *Meas. Sci. Technol.* **2021**, *32*, 125106. [[CrossRef](#)]

20. Leng, J.; Asundi, A. Structural health monitoring of smart composite materials by using EFPI and FBG sensors. *Sens. Actuators A Phys.* **2003**, *103*, 330–340. [[CrossRef](#)]
21. Poeggel, S.; Tosi, D.; Fusco, F.; Ippolito, J.; Lupoli, L.; Mirone, V.; Sannino, S.; Leen, G.; Lewis, E. Fiber-Optic EFPI Pressure Sensors for In Vivo Urodynamic Analysis. *IEEE Sens. J.* **2014**, *14*, 2335–2340. [[CrossRef](#)]
22. Wang, S.; Wang, J.; Li, W.; Liu, Y.; Li, J.; Jia, P. A MEMS-Based High-Fineness Fiber-Optic Fabry–Perot Pressure Sensor for High-Temperature Application. *Micromachines* **2022**, *13*, 763. [[CrossRef](#)]
23. Qi, X.; Wang, S.; Jiang, J.; Liu, K.; Wang, X.; Yang, Y.; Liu, T. Fiber Optic Fabry-Perot Pressure Sensor with Embedded MEMS Micro-Cavity for Ultra-High Pressure Detection. *J. Light. Technol.* **2019**, *37*, 2719–2725. [[CrossRef](#)]
24. Gutierrez-Rivera, M.; Jauregui-Vazquez, D.; Garcia-Mina, D.F.; Sierra-Hernandez, J.M.; Estudillo-Ayala, J.M.; Almanee, M.; Rojas-Laguna, R. Fiber Optic Fabry-Perot Micro-Displacement Sensor Based on Low-Cost Polymer Film. *IEEE Sens. J.* **2020**, *20*, 4719–4725. [[CrossRef](#)]
25. Li, A.; Jing, Z.G.; Liu, Y.Y.; Liu, Q.; Huang, Z.Y.; Cheng, Y.; Zhang, Y.; Han, M.; Peng, W. Quadrature operating point stabilizing technique for fiber-optic Fabry–Perot sensors using vernier-tuned distributed Bragg reflectors laser. *IEEE Sens. J.* **2021**, *21*, 2084–2091. [[CrossRef](#)]
26. Wang, T.T.; Wang, M.; Li, M.; Lu, M. Dual-wavelength demodulation and wavelength optimization for optical fiber Fabry-Perot sensor. *Acta Opt. Sin.* **2005**, *10*, 3–7.
27. Murphy, K.A.; Gunther, M.F.; Wang, A.; Claus, R.O.; Vengsarkar, A.M. Extrinsic Fabry-Perot optical fiber sensor. In Proceedings of the 8th Optical Fiber Sensors Conference, Monterey, CA, USA, 29–31 January 1992.
28. Huang, L.R.; Wang, W.; Wang, Z.; Dong, X.L.; Liu, B. Research on DC compensation demodulation technology for optical fiber F-P sound pressure sensor. *J. Astronaut. Metrol. Meas.* **2022**, *42*, 50–54.
29. Wu, Y.; Xia, L.; Wu, N.S.; Wang, Z.Y.; Zuo, G.M. Optimized feedforward neural network for multiplexed extrinsic Fabry-Perot sensors demodulation. *J. Light. Technol.* **2021**, *39*, 4564–4569. [[CrossRef](#)]
30. Tao, J.; Chen, Y.L.; Lu, J.Q. Method of the cavity length demodulation for optical fiber F-P sensors based on sparse fast Fourier transform. *Chin. J. Lasers* **2018**, *5*, 222–228.
31. Mei, J.W.; Xiao, X.S.; Yang, C.X. High-resolution and large dynamic range fiber extrinsic Fabry–Perot sensing by multi-extrema-tracing technique. *Appl. Opt.* **2015**, *54*, 3677–3681. [[CrossRef](#)]
32. Cao, Q.; Jia, P.G.; Yang, B.; Zhang, H.R.; Hong, Y.P.; Xiong, J.J. Study of improved algorithm about data demodulation of fiber optic F-P pressure sensing system. *Instrum. Tech. Sens.* **2015**, *12*, 15–18.
33. Zhang, P. Research on Demodulation Technology of Short-Cavity Interferometric Fiber Optic Fabry-Perot Pressure Sensors. Master’s Thesis, Nanjing University of Information Science and Technology, Nanjing, China, 2021.
34. Lin, Q.; Chen, L.H.; Li, S.; Wu, X. A high-resolution fiber optic accelerometer based on intracavity phase-generated carrier (PGC) modulation. *Meas. Sci. Technol.* **2011**, *22*, 015303. [[CrossRef](#)]
35. Hou, C.B.; Guo, S. Automatic carrier phase delay synchronization of PGC demodulation algorithm in fiber-optic interferometric sensors. *KSII Trans. Internet Inf. Syst.* **2020**, *14*, 2891–2903.
36. Jia, J.S.; Jiang, Y.; Gao, H.C.; Zhang, L.C.; Jiang, Y. Three-wavelength passive demodulation technique for the interrogation of EFPI sensors with arbitrary cavity length. *Opt. Express* **2019**, *27*, 8890–8899. [[CrossRef](#)] [[PubMed](#)]
37. Liu, Q.; Jing, Z.G.; Xia, Z.J.; Huang, Z.Y.; Peng, W. Fiber-optic ultrasonic sensing via quasi-continuous quadrature frequency modulation. *IEEE Photonics Technol. Lett.* **2020**, *32*, 1385–1388. [[CrossRef](#)]

Disclaimer/Publisher’s Note: The statements, opinions and data contained in all publications are solely those of the individual author(s) and contributor(s) and not of MDPI and/or the editor(s). MDPI and/or the editor(s) disclaim responsibility for any injury to people or property resulting from any ideas, methods, instructions or products referred to in the content.